

Three-Dimensional Reconstruction for Single-Channel Curvilinear SAR Based on Azimuth Prefocusing

Chenghao Jiang¹, Shiyang Tang¹, *Member, IEEE*, Qi Dong, Yinan Li, *Member, IEEE*, Juan Zhang¹, Guoliang Sun, and Linrang Zhang

Abstract—Unlike the traditional multichannel synthetic aperture radar (SAR) 3-D reconstruction technology, the single-channel SAR with two synthetic apertures in the vertical and horizontal planes, realized by curved trajectory, has the advantages of requiring less acquisition data, lower device cost, and fewer limitations on trajectories. However, due to the complex aerodynamic configuration and flight characteristics, critical challenges are faced, including the mathematical model establishment, signal property analyses, and reconstruction approach design. In this article, to address these issues, a 3-D vector geometry model of the curvilinear SAR (CLSAR) system is presented and its properties, including elevation bandwidth and resolution, are studied in detail. Then, a novel 3-D reconstruction approach for a single-channel CLSAR system based on azimuth prefocusing is presented, in which the cylindrical symmetry of the SAR system is utilized to provide accurate azimuth information of targets in observing scenes. With the assisted azimuths, the scene imaged in the vertical plane can be performed, and the 3-D reconstruction of interested targets can be obtained. Numerical results using simulated data demonstrate the effectiveness of the proposed approach.

Index Terms—3-D reconstruction, azimuth prefocusing, cylindrical symmetry, elevation synthetic aperture.

I. INTRODUCTION

AS A well-known technique that uses range and Doppler information to produce high-resolution images, synthetic

Manuscript received 29 May 2023; revised 26 July 2023 and 15 September 2023; accepted 2 October 2023. Date of publication 10 October 2023; date of current version 24 October 2023. This work was supported in part by the National Natural Science Foundation of China under Grant 61971329, Grant 61701393, and Grant 61671361, in part by the Natural Science Basis Research Plan in Shaanxi Province of China under Grant 2020ZDLGY02-08, in part by the Proof of Concept Foundation of Xidian University Hangzhou Institute of Technology under Grant GNYZ2023XJ0101, and in part by the Fundamental Research Funds for the Central Universities under Grant ZYTS23153. (*Corresponding author: Shiyang Tang.*)

Chenghao Jiang, Shiyang Tang, Juan Zhang, and Linrang Zhang are with the National Key Laboratory of Radar Signal Processing, Xidian University, Xi'an 710071, China, and also with the Collaborative Innovation Center of Information Sensing and Understanding, Xidian University, Xi'an 710071, China (e-mail: chjiang@stu.xidian.edu.cn; sytang@xidian.edu.cn; jzhang@xidian.edu.cn; 734961414@qq.com).

Qi Dong is with Beijing Institute of Control and Electronics Technology, Beijing 100038, China (e-mail: work_buffer@163.com).

Yinan Li is with the National Key Laboratory of Radar Signal Processing, Xidian University, Xi'an 710071, China, and also with China Academy of Space Technology, Xi'an 710100, China (e-mail: liyn@cast504.com).

Guoliang Sun is with AVIC Leihua Electronic Technology Research Institute, Wuxi 214000, China (e-mail: sunground@gmail.com).

Digital Object Identifier 10.1109/JSTARS.2023.3323521

aperture radar (SAR) has been widely adopted in diverse fields, including air-to-ground imaging of objects, terrain, and oceans [1]. Based on the assumption of a linear flight path with certain height [2], [3], [4], a 2-D SAR image is obtained by the synthetic aperture in the azimuth direction and the large time-bandwidth product signal in the range direction. Employing 2-D SAR images to construct a 3-D illuminated scene results in a layover phenomenon, image distortion, and lack of target elevation information, which greatly limits its practical implementation [5], [6], [7]. Thus, 3-D SAR techniques, which could extract the accurate 3-D coordinates of targets, are preferred [8], [9]. Currently, 3-D SAR is mainly used for reconnaissance, disaster prediction, and urban mapping but still is not extensively applied because of its limitations, including the lack of elevation sampling data and the strict requirements of radar systems and platforms [10].

Several realizations for 3-D SAR have been studied, including the interferometric SAR (In-SAR), multibaseline (or multipass) SAR, and curvilinear SAR (CLSAR), which are elaborated as follows.

- 1) *In-SAR*: By exploiting two antennas to illuminate a fixed scene with two slightly different view angles, as shown in Fig. 1(a), In-SAR can obtain the 2-D SAR image with elevation information. According to the imaging geometry of the In-SAR system, the ground elevation profile is related to the SAR interferometric phase through a known mapping. Thus, the In-SAR technique can be utilized to estimate the altimetric profile [12]. However, the targets distributed along the elevation direction cannot be focused by the single-baseline interferometric technique, which means that the In-SAR technique can only estimate the absolute elevation of the target but without elevation resolution [13], [14], [15].
- 2) *Multibaseline (or multipass) SAR*: The multibaseline SAR is also called the tomography SAR (Tomo-SAR), which is an extension of In-SAR, as shown in Fig. 1(b). The Tomo-SAR system can form a 2-D synthetic aperture at the azimuth-elevation plane by employing several multipass acquisitions over the same area to provide the capability of 3-D resolution [15]. However, the acquisition numbers in the elevation direction cannot always meet the requirement of the Nyquist sampling theorem [16], [17]. Furthermore, the possible nonuniform spatial samples in elevation direction pose great challenges to the processing approaches. In

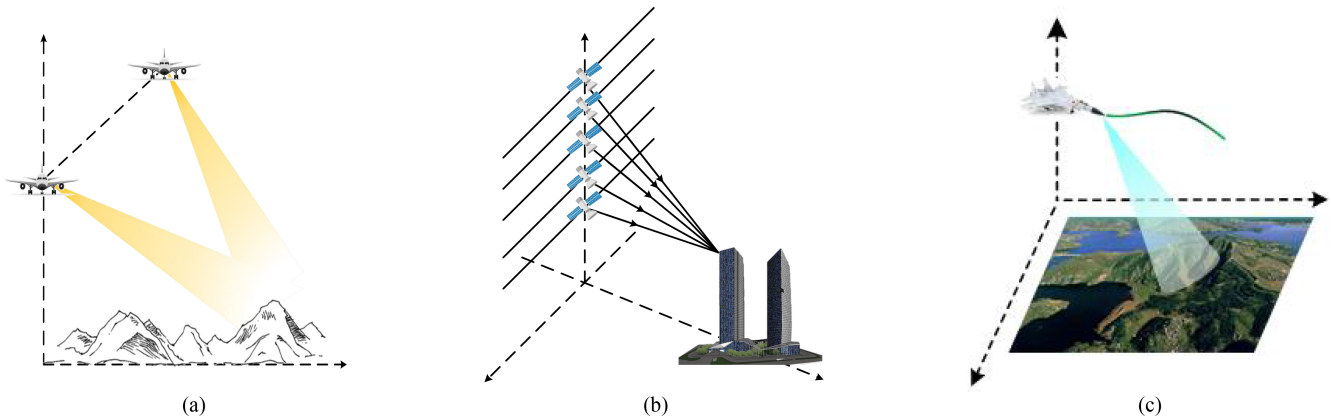


Fig. 1. 3-D SAR imaging systems. (a) In-SAR. (b) Tomo-SAR. (c) CLSAR.

general, these two problems greatly limit the applicability of Tomo-SAR [18], [19], [20].

- 3) *CLSAR*: CLSAR is more applicable than those of the In-SAR and Tomo-SAR because of the single-channel and the single pass [23], [24], as shown in Fig. 1(c). CLSAR provides a high-range resolution by transmitting wideband signal as well as high azimuth and elevation resolutions by 2-D synthetic apertures formed by the curved flight path. However, the echo data collected with curvilinear flight are sparse on the vertical plane and cannot be focused by conventional approaches [25]. To deal with this problem, several spectral estimation methods including RELAX [26], [27], [28] and coherent CLEAN [29], [30], [31] are suggested to extract the 3-D features of targets in small scenes. However, these methods for CLSAR are only employed to estimate the 3-D coordinates of the ideal targets from echo signal but cannot reconstruct the complex 3-D scene, which greatly limits the reconstruction accuracy and the application value [32], [33].

To solve the problem brought by CLSAR, the mathematical model and signal properties are first analyzed with 3-D vector parameters, which indicate that the conventional expressions of the Doppler bandwidth and resolution are both invalid for CLSAR. Moreover, a novel 3-D reconstruction approach based on azimuth pre-focusing is introduced. With the prior information obtained by azimuth pre-focusing, the elevation synthetic aperture of CLSAR can be utilized to obtain SAR images in elevation direction and the accurate 3-D reconstruction result of interested targets can be obtained.

In summary, the novelties and contributions of this work are mainly reflected in two aspects: First, the existing literature has only focused on analyzing certain specific curved trajectory SAR systems without providing a unified and descriptive characterization of the CLSAR system. Addressing this issue, a novel 3-D vector model is established in our work. On this basis, an accurate expression of elevation resolution and bandwidth is analyzed and derived, which is accurate and applicable to any trajectory of the CLSAR system. Second, a novel 3-D reconstruction approach for the CLSAR system is proposed, which can accurately obtain the elevation image and 3-D reconstruction

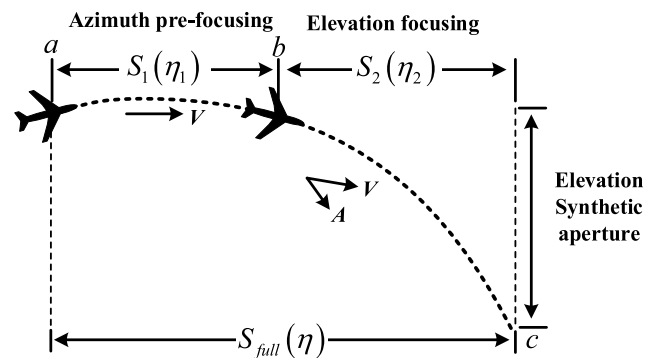


Fig. 2. Curved trajectory suitable for 3-D reconstruction.

result of the interested targets. Compared with the conventional 3-D BP algorithm, the proposed approach significantly reduces the computational burden by eliminating a large number of non-target regions through azimuth pre-focusing, which effectively enhances the practical value of the 3-D CLSAR system.

The rest of this article is organized as follows. In Section II, the geometric model of the CLSAR system is established by using the 2-D Taylor series expansion, and the vector expression of the echo signal is derived. The signal properties of CLSAR are analyzed in Section III. The 3-D reconstruction approach based on azimuth pre-focusing is proposed in Section IV. Section V presents numerical simulation results to evaluate our approach. Finally, Section VI, concludes this article.

II. GEOMETRIC MODEL OF CLSAR

A. Design of the Curved Trajectory

First, a curved trajectory suitable for the 3-D reconstruction of targets for single-channel CLSAR is designed, which is shown in Fig. 2. Note that the full curved synthetic aperture designed for the 3-D reconstruction of targets consists of two subapertures, ab and bc , respectively. The subaperture ab is a smooth motion trajectory without elevation and velocity variable, which is utilized to obtain the azimuth pre-focusing result and extracting azimuth assistance information of the interested targets. On the other

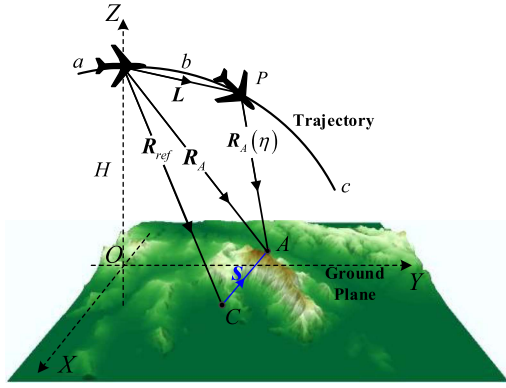


Fig. 3. Geometry of 3-D CLSAR.

hand, during the subaperture bc , the radar platform flies along a large maneuvering curved trajectory, which generates elevation synthetic aperture through elevation variation in the 3-D space, enabling the acquisition of target elevation information.

B. 3-D Vector Geometry Model

The 3-D vector geometry model corresponding to the CLSAR is shown in Fig. 3. Projection of radar location on the ground is assumed to be the origin of the Cartesian coordinate system O - XYZ and H is defined as the initial elevation position of the radar platform. The whole curvilinear synthetic aperture is divided into two subapertures, which are used for azimuth pre-focusing and elevation imaging, respectively. Point C is chosen as the central reference target and \mathbf{R}_{ref} denotes the reference slant vector. Thus, the slant range history $\mathbf{R}_A(\eta)$ corresponding to the arbitrary target A is expressed as

$$\mathbf{R}_A(\eta) = \mathbf{R}_A - \mathbf{L} = \begin{cases} \mathbf{R}_{\text{ref}} + \mathbf{s} - \mathbf{V}\eta, & \eta < \eta_1 \\ \mathbf{R}_{\text{ref}} + \mathbf{s} - \mathbf{V}\eta + \mathbf{A}\eta^2/2, & \eta_1 \leq \eta \leq \eta_2 \end{cases} \quad (1)$$

Depending on different purposes, η_1 and η_2 are the azimuth and elevation slow times of two subapertures. \mathbf{V} and \mathbf{A} are, respectively, the velocity and acceleration vectors, \mathbf{R}_A denotes the initial slant range vector from A to the platform, \mathbf{s} represents the vector from C to A , and $|\cdot|$ is the absolute value operator. The 2-D Taylor series expansion is given by

$$\begin{aligned} \mathbf{R}_A(\eta) &= R_{\text{Sca}}(\eta) + R_{\text{Vec}}(\eta) \\ &= \sum_{n=0} \frac{1}{n!} \mu_n \cdot \eta^n + \sum_{n=0} \frac{1}{n!} \langle \omega_n, \mathbf{S} \rangle \cdot \eta^n \end{aligned} \quad (2)$$

where the initial slant range is decomposed into two parts: the scalar one $R_{\text{Sca}}(\eta)$, which is the same in the traditional SAR, and the vectorial component $R_{\text{Vec}}(\eta)$ that caused by the curved path. μ_n and ω_n are, respectively, the scalar and vectorial coefficients, which are described in Table I. Note that two main impacts due to the acceleration \mathbf{A} should be considered. One is the Doppler parameters, including the bandwidth and resolution, change greatly and another is the deteriorated space variations.

TABLE I
VELOCITY AND ANGLE PARAMETERS

Symbol	Quantity
$\mu_0(\mathbf{R}_{\text{ref}})$	reference slant range
$\mu_1(\mathbf{R}_{\text{ref}})$	rotational velocity
$\mu_2(\mathbf{R}_{\text{ref}})$	rotational acceleration
$\mu_3(\mathbf{R}_{\text{ref}})$	rate of rotational acceleration
$\omega_0(\mathbf{R}_{\text{ref}}) = \nabla \mu_0(\mathbf{R}_{\text{ref}})$	unit vector of reference slant range
$\omega_1(\mathbf{R}_{\text{ref}}) = \nabla \mu_1(\mathbf{R}_{\text{ref}})$	angular velocity vector
$\omega_2(\mathbf{R}_{\text{ref}}) = \nabla \mu_2(\mathbf{R}_{\text{ref}})$	angular acceleration vector
$\omega_3(\mathbf{R}_{\text{ref}}) = \nabla \mu_3(\mathbf{R}_{\text{ref}})$	rate of angular acceleration vector

With range history in (2), the baseband echo signal of A can be expressed as

$$\begin{aligned} S_{\text{Full}}(\tau, \eta) &= \sigma_A \cdot \omega_\tau \left[\tau - \frac{2R(\eta)}{c} \right] \cdot \omega_\eta \left(\frac{\eta - \eta_C}{T} \right) \\ &\quad \cdot \exp \{ -j4\pi [R_{\text{Sca}}(\eta) + R_{\text{Vec}}(\eta)] / \lambda \} \\ &\quad \cdot \exp \left\{ j\pi \gamma \left[\tau - 2(R_{\text{Sca}}(\eta) + R_{\text{Vec}}(\eta)) / c \right]^2 \right\} \end{aligned} \quad (3)$$

where $\omega_\tau(\cdot)$ and $\omega_\eta(\cdot)$ denote the window functions of fast time and slow time, respectively, T represents the synthetic time, η_C is the beam center time of reference point C , λ is the wavelength, and c is the speed of light.

As shown in Fig. 3, the original echo signal $S_{\text{Full}}(\tau, \eta)$ is consists of the horizontal and vertical components $S_1(\tau, \eta_1)$ and $S_2(\tau, \eta_2)$, respectively, according to the different radar flight path, which is given by

$$S_{\text{Full}}(\tau, \eta) = S_1(\tau, \eta_1) + S_2(\tau, \eta_2) \quad (4)$$

where $S_1(\tau, \eta_1)$ is the echo signal corresponding to a short subaperture with small elevation variation (from point a to b) and is utilized for azimuth pre-focusing with η_1 being the corresponding slow time. However, $S_2(\tau, \eta_2)$ is the echo signal of radar platform with large elevation variation (from points b to c) and is utilized for elevation focusing with η_2 being the corresponding slow time in elevation focusing processing. These two parts are employed for image formation and reconstruction in the horizontal and vertical planes.

III. PARAMETER PROPERTIES

The SAR system parameters, including the Doppler bandwidth and resolutions, are very important to the SAR imaging system analysis [34]. Unlike the straight path SAR system that only has azimuth synthetic aperture, the 3-D CLSAR imaging system needs to form azimuth synthetic aperture and elevation synthetic aperture within one flight to provide azimuth and elevation resolutions. Thus, the flight path must be curved, which means that the analyses of the 3-D CLSAR system are much more complicated than the straight path case [35]. However,

existing studies have not yet analyzed an expression for elevation resolution that is applicable to arbitrary CLSAR systems. Therefore, in this section, the resolution calculation in various directions, particularly in the elevation direction of the CLSAR system, is analyzed based on the established 3-D vector model.

A. Properties in Azimuth Direction

First, the azimuth prefocusing system is utilized to provide the assisted azimuth of all targets in the imaging scene. Thus, the azimuth bandwidth and resolution are analyzed.

1) *Azimuth Bandwidth*: In the azimuth prefocusing system, the instantaneous Doppler frequency can be expressed as

$$f_{\text{ins}}(\eta_1) = \frac{2|\mathbf{V}_{\text{ins}}(\eta_1)| \cdot \sin[\theta_{\text{ins}}(\eta_1)]}{\lambda} \quad (5)$$

where $|\mathbf{V}_{\text{ins}}(\eta_1)| = \sqrt{V_x^2(\eta_1) + V_y^2(\eta_1)}$ denotes the magnitude of the instantaneous velocity vector at slow time η_1 , while V_x and V_y are the components of the instantaneous velocity vector in range and azimuth directions, respectively. θ_{ins} represents the instantaneous angle between the instantaneous velocity vector and the instantaneous slant range vector. Thus, the azimuth bandwidth of the azimuth prefocusing system is

$$\begin{aligned} B_{\text{azi}} &= \max\{f_{\text{ins}}\} - \min\{f_{\text{ins}}\} \\ &= \left| -\frac{4}{\lambda} \cdot \frac{\langle \mathbf{V}, \mathbf{V} \rangle}{2|\mathbf{R}_{\text{ref}}|} \cdot \Delta T_m \right| + \left| -\frac{4}{\lambda} \cdot \frac{\langle \mathbf{V}, \mathbf{V} \rangle}{2|\mathbf{R}_{\text{ref}}|} \cdot \Delta T_A \right| \\ &= B_{\text{DC}} + \Delta B_{\text{BW}} \end{aligned} \quad (6)$$

where $\Delta T_A = \theta_{\text{azi}} \cdot |\mathbf{R}_{\text{ref}}|/|\mathbf{V}|$ denotes the equivalent integration time of an azimuth beamwidth, ΔT_m denotes the synthetic time of the radar platform, and θ_{azi} represents the azimuth beamwidth. B_{DC} and ΔB_{BW} are the azimuth Doppler bandwidth and azimuth beam bandwidth, respectively.

2) *Azimuth Resolution*: The Doppler modulation rate of the azimuth prefocusing system, as shown in (6), can be expressed as $k_a = \frac{-2 \cdot |\mathbf{V}_r|^2}{\lambda \cdot |\mathbf{R}_{\text{ref}}|}$, where $\mathbf{V}_r = \langle \mathbf{V}, \mathbf{U}_s \rangle$ and \mathbf{U}_s represents the unit vector of the slant range from targets to radar. Thus, the azimuth resolution of the azimuth prefocusing system is

$$\rho_a = \frac{|\mathbf{V}_r|}{B_{\text{azi}}} = \frac{|\mathbf{V}_r|}{|k_a \cdot (\Delta T_E + \Delta T_m)|} \quad (7)$$

B. Properties in Elevation Direction

The elevation SAR image will be focused on the selected vertical plane that confirms the assisted azimuth. Because the 3-D velocity vector and acceleration vector cannot be ignored in the CLSAR system, the traditional 2-D calculation method used in a straight path SAR system will result in a large error in the elevation focusing system. Thus, it is necessary to analyze the accurate elevation bandwidth and resolution of a single-channel 3-D CLSAR system in detail.

1) *Elevation Bandwidth*: In this section, the total bandwidth in the elevation dimension of the CLSAR system is analyzed. The instantaneous Doppler frequency can be expressed as

$$f_{\text{ins}} = \frac{2|\mathbf{V} + \mathbf{A}\eta| \cdot (f_c + f_r) \sin(\theta_{\text{ins}} - \Delta\theta)}{c} \quad (8)$$

where f_c and f_r are the carrier frequency and the range frequency, respectively, and $\Delta\theta \in [-\theta_{\text{ele}}/2, \theta_{\text{ele}}/2]$ with θ_{ele} being the elevation beamwidth. The total bandwidth of the elevation focusing system is

$$\begin{aligned} B_{\text{ele}} &= \max\{f_{\text{ins}}\} - \min\{f_{\text{ins}}\}c \\ &= \left| -\frac{4}{\lambda} \cdot \mu_2 \cdot \Delta T_E \right| + \left| -\frac{4}{\lambda} \cdot \mu_2 \cdot \Delta T_m \right| \\ &\quad + \frac{2B_r}{c} \mu_1 \cos(\theta_{\text{pit}}) \\ &= \left| -\frac{4}{\lambda} \cdot \left(\frac{|\mathbf{V}|^2 - \langle \mathbf{A}, \mathbf{R}_{\text{ref}} \rangle}{|\mathbf{R}_{\text{ref}}|} - \frac{\langle \mathbf{V}, \mathbf{R}_{\text{ref}} \rangle^2}{|\mathbf{R}_{\text{ref}}|^3} \right) \cdot \Delta T_m \right| \\ &\quad + \left| -\frac{4}{\lambda} \cdot \left(\frac{|\mathbf{V}|^2 - \langle \mathbf{A}, \mathbf{R}_{\text{ref}} \rangle}{|\mathbf{R}_{\text{ref}}|} - \frac{\langle \mathbf{V}, \mathbf{R}_{\text{ref}} \rangle^2}{|\mathbf{R}_{\text{ref}}|^3} \right) \cdot \Delta T_E \right| \\ &\quad + \frac{2B_r}{c} \frac{\langle \mathbf{V}, \mathbf{R}_{\text{ref}} \rangle}{|\mathbf{R}_{\text{ref}}|} \cos(\theta_{\text{pit}}) \\ &= B_{\text{dc}} + \Delta B_{\text{bw}} + \Delta B_{\text{pit}}. \end{aligned} \quad (9)$$

Note that the elevation bandwidth B_{ele} is composed of the elevation Doppler center bandwidth B_{dc} , elevation beam bandwidth ΔB_{bw} , and pitched bandwidth ΔB_{pit} , respectively. B_{dc} is generated due to the platform motion and affected by the synthetic time ΔT_m , while ΔB_{bw} results from the offset of the Doppler center of elevation spectrum when the scatterers elevation position is not at the scene center, and its value is determined by the equivalent integration time $\Delta T_E = \theta_{\text{ele}} \cdot |\mathbf{R}_{\text{ref}}|/|\mathbf{V}|$, where θ_{ele} represents the elevation beamwidth of the transmitted signal. ΔB_{pit} is caused by the presence of the pitch angle, leading to a tilting widening of the system's Doppler spectrum in the elevation direction, and its value is jointly determined by the range bandwidth B_r and pitch angle θ_{pit} . Other parameters are the same as the azimuth prefocusing system.

Apparently, according to the expression of total bandwidth in elevation dimension, both $\mu_2 = \frac{|\mathbf{V}|^2 - \langle \mathbf{A}, \mathbf{R}_{\text{ref}} \rangle}{|\mathbf{R}_{\text{ref}}|} - \frac{\langle \mathbf{V}, \mathbf{R}_{\text{ref}} \rangle^2}{|\mathbf{R}_{\text{ref}}|^3}$ and ΔT_m are dependent on acceleration. Thus, the elevation beam bandwidth ΔB_{bw} and the elevation Doppler center bandwidth B_{dc} are both affected by acceleration terms, which is different from the expression in the azimuth prefocusing system. It is well known that even a small variation of acceleration could greatly affect the total elevation bandwidth. Furthermore, in order to get high resolution at both azimuth and elevation dimensions, the CLSAR system is a spotlight mode SAR. Thus, the whole acquisition interval ΔT_m is much longer than the straight path SAR system, and B_{ele} may span over several pulse-repetition frequency (PRF) intervals, which will cause Doppler spectrum wrapping. Moreover, the pitched bandwidth ΔB_{pit} also cannot be ignored and may lead to the Doppler spectrum backfolding. Thus, the total elevation bandwidth gets larger in this case. Based on the sampling requirement, the PRF of the elevation focusing system must be larger than the total elevation bandwidth to avoid spectral aliasing.

2) *Along-Track and Cross-Track Resolutions*: Affected by the 3-D velocity vector and acceleration vector, the traditional

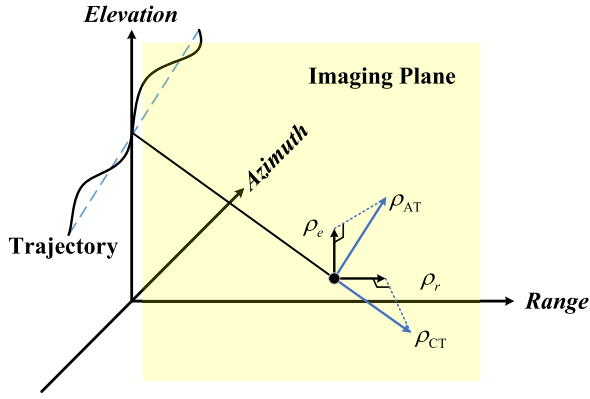


Fig. 4. Direction of each resolution.

analysis and calculation methods of resolution are not suitable for the elevation focusing system without any modifications. The most comprehensive information regarding the SAR resolution can be obtained by the ambiguity function (AF). The traditional calculation method decomposes the AF expression, neglecting the impact of higher-order terms, which allows AF to be split into two independent functions for separate calculations of azimuth and range resolutions. However, due to the complex 3-D motion parameters and irregular trajectory directions of the CLSAR system, the impact of higher-order terms cannot be ignored, leading to the ineffectiveness of this method. To address this issue, several approximation methods have been proposed. Studies in [36] and [37] have found that the AF plot has a parabolic shape between points 0 and -3 dB and can be approximated by quartic polynomials. However, the accuracy of these approaches is affected by various parameters, such as orbit position, integration time, and azimuth angle, which limit its applicability. Moreover, the computational complexity of AF in CLSAR is very high. In SAR, a linear frequency modulation signal is transmitted, which can measure differences in time delay and Doppler frequency. Imaging performance depends on the capability of translating these differences in different detected areas. Thus, the spatial resolution of the CLSAR system is divided into along-track one ρ_{AT} and cross-track one ρ_{CT} , which is analyzed by the Doppler frequency differences and time delay, respectively. The directions of each resolution are shown in Fig. 4, where ρ_r and ρ_e are fast- and slow-time resolutions on the vertical plane.

Cross-Track Resolution: According to the vector geometry model shown in Fig. 3, the path delay time between the arbitrary target A and reference target C is

$$t_d(\eta, \mathbf{R}_{\text{ref}}) = \frac{2}{c} [|\mathbf{r}(\eta, \mathbf{s}; \mathbf{R}_{\text{ref}})| - |\mathbf{r}(\eta, 0; \mathbf{R}_{\text{ref}})|] \quad (10)$$

then performing gradient operation on the delay time $t_d(\eta, \mathbf{R}_{\text{ref}})$ with respect to the variation $|\mathbf{r}(\eta, \mathbf{s}; \mathbf{R}_{\text{ref}})|$, the expression can be represented as

$$\begin{aligned} & \nabla(t_d(\eta, \mathbf{R}_{\text{ref}})) \\ &= \frac{2}{c} [\nabla|\mathbf{r}(\eta, \mathbf{s}; \mathbf{R}_{\text{ref}})| - \nabla|\mathbf{r}(\eta, 0; \mathbf{R}_{\text{ref}})|] |_{\mathbf{s}=0} \\ &= \frac{2}{c} \mathbf{U}_r(\eta; \mathbf{R}_{\text{ref}}) \end{aligned} \quad (11)$$

where \mathbf{U}_r is the unit vector from the arbitrary target A to the radar platform P in the range gradient direction, and $\mathbf{U}_r(\eta; \mathbf{R}_{\text{ref}}) = (\mathbf{R}_{\text{ref}} - \mathbf{V}\eta - \frac{1}{2}\mathbf{A}\eta^2)/|\mathbf{r}(\eta, 0; \mathbf{R}_{\text{ref}})|$. By viewing the expression, it can be found that the essence of the gradient operation is to measure the variation of the delay time t_d , which is affected by the slant range vector \mathbf{r} and can be represented as

$$d(t_d) = \nabla(t_d) \cdot d(\mathbf{r}) \quad (12)$$

where d denotes the differential operator. Obviously, the gradient of t_d represents the direction that maximizes the change in delay time difference. Thus, the cross-track resolution (-3 dB width) of the CLSAR system can be computed as

$$\rho_{CT} = \frac{d(t_d)}{\nabla(t_d)} = \frac{1}{|\frac{2}{c}\mathbf{U}_r(\eta; \mathbf{R}_{\text{ref}})| \cdot B_r} \quad (13)$$

Along-Track Resolution: According to the vector geometry model shown in Fig. 3, the phase history difference between arbitrary target A and reference target C is

$$\varphi_d(\eta; \mathbf{R}_{\text{ref}}) = \frac{4\pi}{\lambda} [|\mathbf{r}(\eta, \mathbf{s}; \mathbf{R}_{\text{ref}})| - |\mathbf{r}(\eta, 0; \mathbf{R}_{\text{ref}})|] \quad (14)$$

After taking the derivative of the phase difference φ_d , the Doppler frequency can be derived as

$$\begin{aligned} f_D(\eta; \mathbf{R}_{\text{ref}}) &= \frac{1}{2\pi} \cdot \frac{\partial \varphi(\eta; \mathbf{R}_{\text{ref}})}{\partial \eta} \\ &= \frac{2}{\lambda} \cdot \left[\frac{\partial |\mathbf{r}(\eta, \mathbf{s}; \mathbf{R}_{\text{ref}})|}{\partial \eta} - \frac{\partial |\mathbf{r}(\eta, 0; \mathbf{R}_{\text{ref}})|}{\partial \eta} \right] \end{aligned} \quad (15)$$

then performing gradient operation on the Doppler frequency $f_D(\eta; \mathbf{R}_{\text{ref}})$ with respect to the variation $|\mathbf{r}(\eta, 0; \mathbf{R}_{\text{ref}})|$, we have

$$\begin{aligned} \nabla f_D(\eta; \mathbf{R}_{\text{ref}}) &= -\frac{2}{\lambda} \cdot \frac{1}{|\mathbf{r}(\eta, 0; \mathbf{R}_{\text{ref}})|} \cdot [(\mathbf{V} + \mathbf{A}\eta) \\ &\quad - \langle (\mathbf{V} + \mathbf{A}\eta), \mathbf{U}_r(\eta; \mathbf{R}_{\text{ref}}) \rangle \cdot \mathbf{U}_r(\eta; \mathbf{R}_{\text{ref}})] \end{aligned} \quad (16)$$

To obtain high resolution, the integration time of the elevation focusing system must be long. Thus, according to (16), the acceleration vector has a significant impact on the Doppler frequency difference, which cannot be ignored in resolution analysis.

Employing the physical method and the expression of Doppler frequency difference in (16), the spatial angular variable vector of the radar platform can be expressed as

$$\omega_D(\eta; \mathbf{R}_{\text{ref}}) = \frac{\lambda \cdot \nabla f_D(\eta; \mathbf{R}_{\text{ref}})}{2} \quad (17)$$

Thus, on the basis of relations between coherent angle and resolution, the along-track resolution (-3-DB width) can be expressed as

$$\begin{aligned} \rho_{AT} &= \frac{\lambda}{\left| 2 \int_{\eta_0}^{\eta_1} \omega_D(\eta; \mathbf{R}_{\text{ref}}) d\eta \right|} = \frac{\lambda}{\left| 2 \int_{\eta_0}^{\eta_1} \nabla \frac{\partial |\mathbf{r}(\eta, 0; \mathbf{R}_{\text{ref}})|}{\partial \eta} \cdot d\eta \right|} \\ &= \frac{\lambda}{\left| 2 \int_{\eta_0}^{\eta_1} \frac{\partial (\nabla |\mathbf{r}(\eta, 0; \mathbf{R}_{\text{ref}})|)}{\partial \eta} \cdot d\eta \right|} \end{aligned}$$

$$\begin{aligned}
&= \frac{\lambda}{2 |\nabla |\mathbf{r}(\eta_1, 0; \mathbf{R}_{\text{ref}})| - \nabla |\mathbf{r}(\eta_0, 0; \mathbf{R}_{\text{ref}})||} \\
&= \frac{\lambda}{2 |\mathbf{U}_r(\eta_1; \mathbf{R}_{\text{ref}}) - \mathbf{U}_r(\eta_0; \mathbf{R}_{\text{ref}})|} \quad (18)
\end{aligned}$$

where η_0 and η_1 are the start time and end time of the synthetic aperture formed by the radar platform.

3) *Fast- and Slow-Time Resolutions on Vertical Plane*: It is clear that the resolutions derived in (13) and (15) are the spatial resolutions of CLSAR, which are provided by the transmitted signal and spatial curved synthetic aperture. The values and directions of them will vary with changes in the platform and system parameters. Since the subsequent 3-D reconstruction needs to obtain the imaging results on the elevation imaging plane, the optimal fast- and slow-time resolutions on the elevation imaging plane should be analyzed.

Assume that the spatial resolution space of CLSAR is spanned by two orthogonal unit vectors $\alpha_{\text{spa}} = \mathbf{U}_r(\eta_{\text{ref}}; \mathbf{R}_{\text{ref}})$ and $\beta_{\text{spa}} = \mathbf{U}_D(\eta_{\text{ref}}; \mathbf{R}_{\text{ref}})$, where

$$\begin{aligned}
&\mathbf{U}_D(\eta_{\text{ref}}; \mathbf{R}_{\text{ref}}) \\
&= \frac{(\mathbf{V} + \mathbf{A}\eta_{\text{ref}})^T \cdot (\mathbf{I} - \mathbf{U}_r(\eta_{\text{ref}}; \mathbf{R}_{\text{ref}}) \cdot \mathbf{U}_r(\eta_{\text{ref}}; \mathbf{R}_{\text{ref}})^T)}{\left| (\mathbf{V} + \mathbf{A}\eta_{\text{ref}})^T \cdot (\mathbf{I} - \mathbf{U}_r(\eta_{\text{ref}}; \mathbf{R}_{\text{ref}}) \cdot \mathbf{U}_r(\eta_{\text{ref}}; \mathbf{R}_{\text{ref}})^T) \right|} \quad (19)
\end{aligned}$$

denotes the unit vector of the Doppler gradient at reference slow time η_{ref} . The vertical plane space is also spanned by two unit vectors α_{ver} and β_{ver} , which are the projections of vectors α_{spa} and β_{spa} on the azimuth plane, respectively, and can be expressed as

$$\alpha_{\text{ver}} = \frac{\alpha_{\text{spa}}^T \cdot (\mathbf{I} - \mathbf{h} \cdot \mathbf{h}^T)}{|\alpha_{\text{spa}}^T \cdot (\mathbf{I} - \mathbf{h} \cdot \mathbf{h}^T)|} \quad (20)$$

$$\beta_{\text{ver}} = \frac{\beta_{\text{spa}}^T \cdot (\mathbf{I} - \mathbf{h} \cdot \mathbf{h}^T)}{|\beta_{\text{spa}}^T \cdot (\mathbf{I} - \mathbf{h} \cdot \mathbf{h}^T)|} \quad (21)$$

where \mathbf{h} is the unit vector along the normal vector direction of the vertical plane. According to the relations in (20) and (21), a transfer matrix \mathbf{H} is

$$\mathbf{H} = \begin{bmatrix} \alpha_{\text{spa}}^T \cdot \alpha_{\text{ver}} & \alpha_{\text{spa}}^T \cdot \beta_{\text{ver}} \\ \beta_{\text{spa}}^T \cdot \alpha_{\text{ver}} & \beta_{\text{spa}}^T \cdot \beta_{\text{ver}} \end{bmatrix}. \quad (22)$$

It is clear that the spatial resolution space can be generated by multiplying the transfer matrix \mathbf{H} and the vertical plane space, which is

$$\begin{bmatrix} r_{\text{spa}} \\ a_{\text{spa}} \end{bmatrix} = \mathbf{H} \cdot \begin{bmatrix} r_{\text{ele}} \\ h_{\text{ele}} \end{bmatrix} \quad (23)$$

where $[r_{\text{spa}}, a_{\text{spa}}]^T$ represents an arbitrary target in the spatial space and $[r_{\text{ele}}, h_{\text{ele}}]^T$ represents the new coordinates in the vertical plane space after the coordinate space transformation. Thus, the fast- and slow-time resolutions in the chosen vertical plane can be derived as

$$\rho_r = \frac{\rho_{\text{CT}}}{\alpha_{\text{spa}}^T \cdot \alpha_{\text{ver}}} \quad (24)$$

$$\rho_e = \frac{\rho_{\text{AT}}}{\beta_{\text{spa}}^T \cdot \beta_{\text{ver}}}. \quad (25)$$

IV. FOCUSING APPROACH

A. Principle and Problem

The cylindrical symmetry of the SAR system needs to be analyzed first, which is the reason that the traditional straight path SAR system cannot be utilized for the 3-D reconstruction [38]. Furthermore, the advantage of the cylindrical symmetry will be presented, which has proved useful for the elevation focusing process in the CLSAR system. After that, the problems of the single-channel CLSAR system using traditional methods to obtain the 3-D SAR image are pointed out. At last, combining the advantages of these two systems, a novel method for the CLSAR 3-D reconstruction based on azimuth prefocusing is proposed.

The imaging principle of the traditional straight path SAR system is illustrated in Fig. 5(a). The platform flies along a linear path with a constant elevation H . Targets P , C , and D are located in the 3D imaging scene, where these three targets are located at the same azimuth cell, targets P and C are located at the same elevation plane (i.e., the ground plane) with different range cell, while targets C and D are located at the same minimum slant range cell but different elevation directions. Thus, the instantaneous slant ranges corresponding to the targets C , D , and P can be expressed as

$$\begin{aligned}
R_C(\eta) &= \sqrt{R_0^2 + (v\eta - y_C)^2} \\
R_D(\eta) &= \sqrt{R_0^2 + (v\eta - y_D)^2} \\
R_P(\eta) &= \sqrt{R_p^2 + (v\eta - y_P)^2} \quad (26)
\end{aligned}$$

where R_0 denotes the minimum slant range from targets C and D to flight path, R_p denotes the minimum slant range of the target P , v is the velocity of the platform of traditional straight path SAR system, η is the slow time, and y_C , y_D , and y_P are the azimuth coordinates of targets C , D , and P , respectively. According to (26), the echo phases of targets C and D are identical. These two targets will be focused at the same location on the 2-D slant range image, implying that cylindrical symmetry can obtain accurate azimuth locations of all targets. In the following elevation focusing processing, the azimuth information will be utilized as assisted information.

Unlike the straight path SAR, the CLSAR system has the capability of elevation image formation. Fig. 5(b) shows the imaging principle of the CLSAR system. Targets are handled the same as in Fig. 5(a) and the platform flies along a curved path. Thus, the instantaneous slant range $|\mathbf{R}(\eta)|$ corresponding to the targets C and D can be expressed as

$$|\mathbf{R}(\eta)| = |\mathbf{R}_0 - \mathbf{L}(\eta)| = |\mathbf{R}_0 - \mathbf{V}\eta - \mathbf{A}\eta^2/2|. \quad (27)$$

This shows that, unlike the straight path SAR system, the instantaneous slant range $|\mathbf{R}(\eta)|$ of targets C and D in the CLSAR system cannot remain constant with the variation of slow time η for the minimum slant range vector \mathbf{R}_0 changing

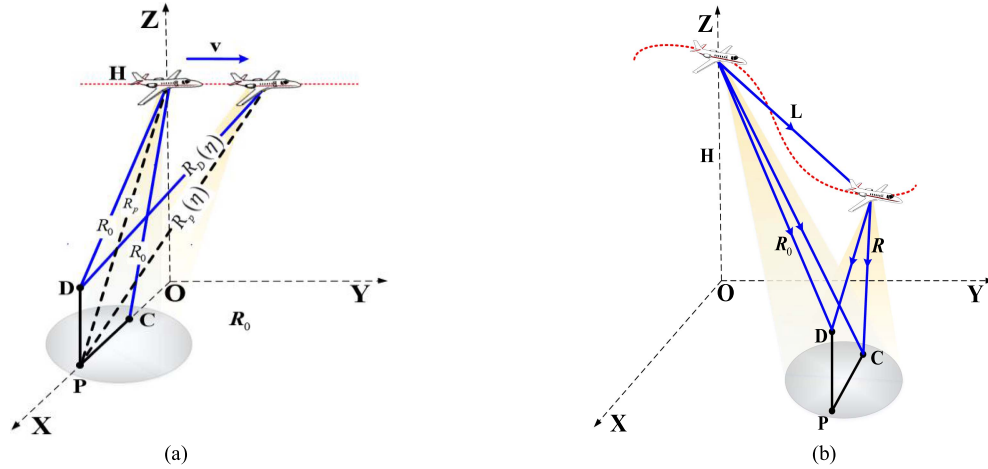


Fig. 5. Imaging principle of the SAR system. (a) Traditional straight path SAR system. (b) CLSAR system.

with the curved flight orbit, which means that targets C and D have a totally different slant range history and echo phase. Thus, these two targets will not be focused at the same pixel as in the traditional SAR system. Note that the CLSAR system does not suffer from cylindrical symmetry.

However, without the cylindrical symmetry, CLSAR systems are normally used to obtain high-resolution 2-D images with its large azimuth aperture [39]. Nevertheless, referring to Fig. 3, the curved orbit cannot only form an azimuth synthetic aperture but also form an elevation aperture within one flight. Thus, the CLSAR can theoretically realize the azimuth and elevation resolution by its 2-D synthetic apertures.

In order to achieve a high-resolution 3-D SAR image, a curved flight orbit should be designed to maximize the dimensions of the frequency space. However, the echo data obtained by curvilinear orbit are always not fully sampled in the vertical plane. Several common curved synthetic apertures formed by CLSAR with single-channel are illustrated in Fig. 6(a)–(c), and the fully sampled synthetic aperture for 3-D SAR systems is shown in Fig. 6(d) for comparison. From Fig. 6(a)–(d), we know that the common aperture of CLSAR with a single channel is a part of a fully sampled aperture. Therefore, the received raw data are sparse in the 3-D space as it is restricted by the shape of the flight orbit. Moreover, if the echo data of the CLSAR system are obtained with a range-Doppler 2-D matrix, such as traditional straight path SAR, it cannot distinguish the sampling in azimuth and elevation dimensions. Hence, it can only form a traditional range-azimuth 2-D image. Furthermore, without the cylindrical symmetry, targets that are not located at the imaging plane will be lost on the 2-D SAR image. If the echo data are collected with a range-azimuth-elevation 3-D matrix, processing these data directly via nonparametric methods, such as fast Fourier transform (FFT) to form 3-D SAR, will produce unusable images suffering from severely high sidelobes. Both parametric methods, such as RELAX and CLEAN algorithms, can avoid this problem. However, they can only estimate the 3-D parameters (i.e., 3-D coordinates and RCS) of ideal point targets or simple targets composed of ideal ones but exhibit poor robustness in complex observation

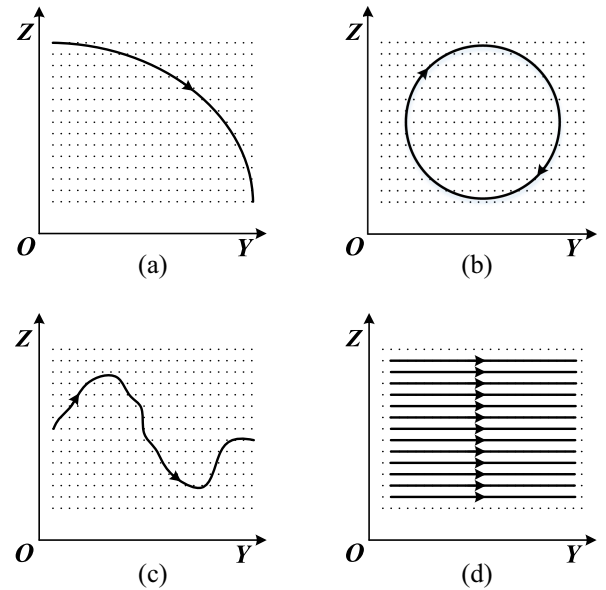


Fig. 6. Common synthetic apertures of CLSAR with single-channel and full sampled aperture. (a) Parabolic aperture. (b) Circular aperture. (c) Arbitrary curved aperture. (d) Full sampled aperture.

scenes. Moreover, these methods require prior knowledge of the number of scatterers in the scene and involve iterative searches, resulting in high computational complexity [40], which greatly limits the 3-D reconstruction accuracy and the application value.

According to the principle and problems analyzed above, we know that the azimuth information obtained from the traditional 2-D SAR image can be used in CLSAR elevation imaging. Thus, in the following section, a novel 3-D reconstruction method for the CLSAR system based on azimuth prefocusing is proposed. With the assisted azimuth obtained from the azimuth prefocusing result, the elevation synthetic aperture of CLSAR can be utilized to obtain the SAR image in elevation direction and the 3-D coordinates of targets can be extracted.

B. Azimuth Prefocusing

First, a 2-D slant range SAR image is focused to provide the assisted azimuth of all targets in the 3-D observing scene, where the subaperture echo data $S_1(\tau, \eta_1)$ are utilized. As an assisted processing, the processing speed must be considered. Hence, a range migration algorithm (RMA) is chosen in this section.

By using the slant range history expressed in (1), the received baseband signal of the azimuth prefocusing system in the range–azimuth 2-D time domain is obtained as

$$S_1(\tau, \eta_1) = \exp \left\{ -j2\pi f_0 \cdot \frac{2|\mathbf{R}(\eta_1)|}{c} \right\} \cdot \exp \left\{ j\pi\gamma \left[\tau - \frac{2|\mathbf{R}(\eta_1)|}{c} \right]^2 \right\} \quad (28)$$

where $|\mathbf{R}(\eta_1)| = |\mathbf{R}_A - \mathbf{V}\eta_1| = \sqrt{(|\mathbf{R}_A| \cos \varphi)^2 + (|\mathbf{R}_A| \sin \varphi - |\mathbf{V}\eta_1|)^2}$ denotes the instantaneous slant range history of arbitrary target A during azimuth prefocusing, \mathbf{R}_A is the initial slant range vector from A to radar platform, φ denotes the slant angle, f_0 denotes the carrier frequency, and γ denotes the range chirp. After being processed by the traditional RMA, the 3-D imaging scene will be projected onto a 2-D slant range plane

$$S_{\text{pre}}(\tau, \eta_1) = \text{sinc} \left[\Delta f_{\tau} \left(\tau - \frac{2|\mathbf{R}|}{c} \right) \right] \cdot \text{sinc} \left[\Delta f_{\eta_1} \left(\eta_1 - \frac{y}{|\mathbf{V}|} \right) \right]. \quad (29)$$

According to (29), one can know that by utilizing the RMA in an azimuth prefocusing process, targets in the 3-D imaging scene are all well-focused at one 2-D slant range image $(|\mathbf{R}|, y)$ without loss. Moreover, because of the cylindrical symmetry, the range $|\mathbf{R}|$ of these targets is inaccurate but the azimuth y is all well-focused. Thus, the azimuth information of interested targets can be extracted from the azimuth prefocusing image by utilizing a target extraction method based on the joint feature function. The function consists of three different features, i.e., brightness, contrast, and image entropy. Specifically, brightness is used to measure the exposure intensity, contrast is used to characterize the feature edges, and image entropy is used to reflect the details and textures. By combining these target features, the robustness of azimuth imaging plane extraction can be effectively guaranteed. The joint feature function is expressed as

$$f(|\mathbf{R}|, y) = \boldsymbol{\alpha} \cdot \mathbf{F} [I_{\text{azi}}(|\mathbf{R}|, y)] \\ = [\alpha_1 \quad \alpha_2 \quad \alpha_3] \begin{bmatrix} F_1 [I_{\text{azi}}(|\mathbf{R}|, y)] \\ F_2 [I_{\text{azi}}(|\mathbf{R}|, y)] \\ F_3 [I_{\text{azi}}(|\mathbf{R}|, y)] \end{bmatrix} \quad (30)$$

where $I_{\text{azi}}(|\mathbf{R}|, y)$ is the 2-D SAR image after azimuth prefocusing, and $\boldsymbol{\alpha}$ denotes the weight vector. $\mathbf{F}[\cdot]$ denotes the joint feature function that contains brightness F_1 , contrast F_2 , and image entropy F_3

$$F_1 [I_{\text{azi}}(|\mathbf{R}|, y)] = \frac{\sum I_{\text{azi}}(|\mathbf{R}|, y)}{N}$$

$$F_2 [I_{\text{azi}}(|\mathbf{R}|, y)] = \sqrt{\frac{\sum \{I_{\text{azi}}(|\mathbf{R}|, y) - F_1 [I_{\text{azi}}(|\mathbf{R}|, y)]\}^2}{N}} \\ F_3 [I_{\text{azi}}(|\mathbf{R}|, y)] = - \sum_{i=0}^{L-1} n_i \log 2(n_i) \quad (31)$$

where N is the number of pixels contained in the entire image, n_i is the number of pixels contained in the i th gray level, and L denotes the gray-scale space. By sliding along the range and azimuth axes, high-value targets can be selected from the cluttered background. Thus, the azimuth imaging plane that utilized for elevation focusing can be obtained.

C. Elevation Focusing

Note that in the traditional straight path SAR system, without variation in elevation direction, the sample of slow time η_1 represents the sample of azimuth synthetic aperture [41]. However, in the CLSAR system, the platform moves not only along the azimuth direction but also along elevation. Therefore, the CLSAR system, regardless of the azimuth, can also form a synthetic aperture at elevation direction. Thus, in this section, the sample of slow time η no longer represents the sample of synthetic aperture at azimuth but the elevation. This ensures that the CLSAR system has elevation resolution. In order to get well-focused elevation images, a highly accurate SAR imaging algorithm, backprojection algorithm (BPA), which does not focus the image on a spatial slant range plane but on a certain azimuth plane, is adopted. The detailed steps of the algorithm are given as follows.

Ignoring the amplitude and phase terms, the received baseband signal of the curved path in the range–elevation 2-D time domains is obtained as

$$S_{\text{Full}}(\tau, \eta) = \exp \left\{ -j2\pi f_0 \cdot \frac{2|\mathbf{R}(\eta)|}{c} \right\} \cdot \exp \left\{ j\pi\gamma \left[\tau - \frac{2|\mathbf{R}(\eta)|}{c} \right]^2 \right\} \quad (32)$$

where $|\mathbf{R}(\eta)| = |\mathbf{R}_A - \mathbf{L}| = |\mathbf{R}_{\text{ref}} + \mathbf{s} - (\mathbf{V}\eta + \mathbf{A}\eta^2/2)|$ denotes the instantaneous slant range history of arbitrary target A of the full curved aperture.

After range compression with $H_{\text{ele-RCM}}(f_{\tau}) = \exp(j\pi f_{\tau}^2/\gamma)$, we have

$$S_2(\tau, \eta) = \text{IFFT} \{ S_{\text{Full}}(\tau, \eta) \cdot H_{\text{ele-RCM}}(f_{\tau}) \} \\ = \text{sinc} \left\{ |\gamma T_p| \left(\tau - \frac{2|\mathbf{R}(\eta)|}{c} \right) \right\} \cdot \exp \left\{ -j \frac{4\pi}{\lambda} |\mathbf{R}(\eta)| \right\} \quad (33)$$

where $S_{\text{Full}}(\tau, \eta)$ is the full-aperture raw echo signal, $\mathbf{R}(\eta)$ is the range history of arbitrary target, γ denotes the range chirp, and T_p denotes the pulsewidth of signal.

Next, according to the assisted azimuth extracted from the 2-D SAR image of azimuth prefocusing, the azimuth plane y_i , which is confirmed to contain targets with different ranges

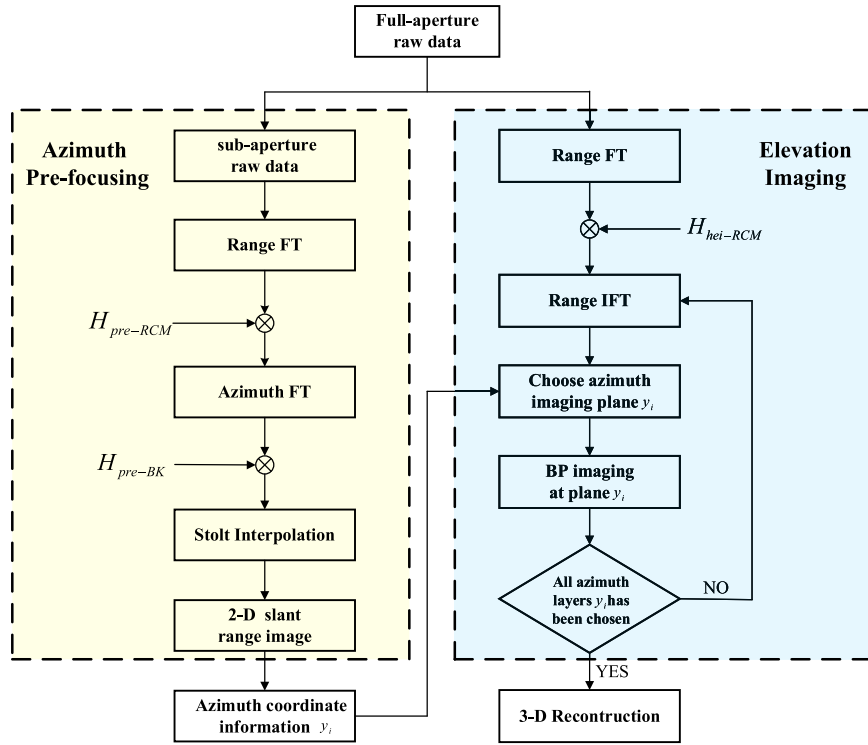


Fig. 7. Flowchart of the 3-D reconstruction approach.

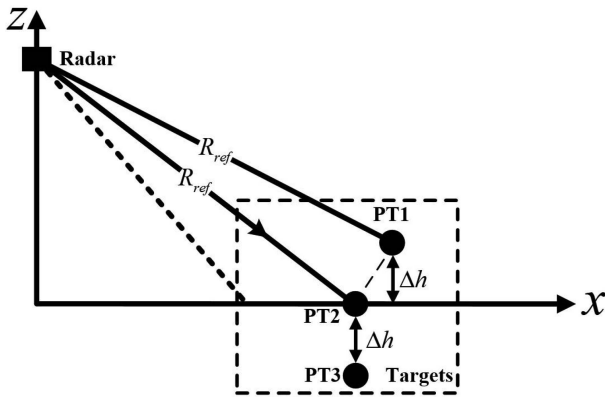


Fig. 8. Geometry of simulated scatterers.

and elevations, has been chosen to be the imaging plane of BPA.

Before imaging, the chosen azimuth plane y_i needs to be divided into a 2-D matrix grid $(\Delta x, \Delta h)$ according to the range-elevation 2-D resolution (i.e., $\Delta x \leq \rho_r$, $\Delta h \leq \rho_h$) of the CLSAR system analyzed in (23) and (24).

For each matrix element on the plane y_i , there is a certain range history function

$$\begin{aligned} |\mathbf{R}(\eta, x_j, y_i, z_j)| &= |\mathbf{R}_A(\eta) - \mathbf{L}| \\ &= |\mathbf{R}_{\text{ref}} - (\mathbf{V}\eta + A\eta^2/2) + \mathbf{s}_i(x_j, z_j)| \end{aligned} \quad (34)$$

where $\mathbf{s}_i(x_j, y_i, z_j)$ denotes the vector from the reference target to any matrix element (x_j, z_j) in the azimuth plane y_i . Using

this range history function, the magnitude of the target located at coordinates (x_j, z_j) can be found from the range compressed signal. After completing the coherent integration of all signals projected to the imaging plane, the range-elevation image on the azimuth plane y_i can be focused as

$$\sigma(x_j, y_i, z_j) = \int_{\eta} S_2(\tau, \eta) \cdot \exp\left\{j\frac{4\pi}{\lambda} |\mathbf{R}(\eta, x_j, y_i, z_j)|\right\} d\eta \quad (35)$$

where $\sigma(x_j, y_i, z_j)$ denotes the pixel value of the targets located at (x_j, y_i, z_j) . Without cylindrical symmetry, only the targets located at plane y_i are well-focused.

At last, after all azimuth planes have been chosen to focus range-elevation images by BPA, the accurate 3-D coordinates of targets can be extracted from the results.

D. Flowchart of the Imaging Approach

The flowchart of the proposed 3-D reconstruction approach based on azimuth prefocusing is shown in Fig. 7. It is worth noting that the left part shows the process flow of azimuth prefocusing and the right part shows the elevation focusing method. The processing procedure of the proposed approach is described as follows.

- 1) *Azimuth prefocusing*: The azimuth prefocusing image is obtained by the echo signal corresponding to a short sub-aperture with a small elevation variation. The dispersion of targets can be corrected by the signal-based phase error compensation method. Accurate azimuth information of targets is then obtained.
- 2) *Elevation focusing*: Use the elevation synthetic aperture of the CLSAR system to focus range-elevation images at

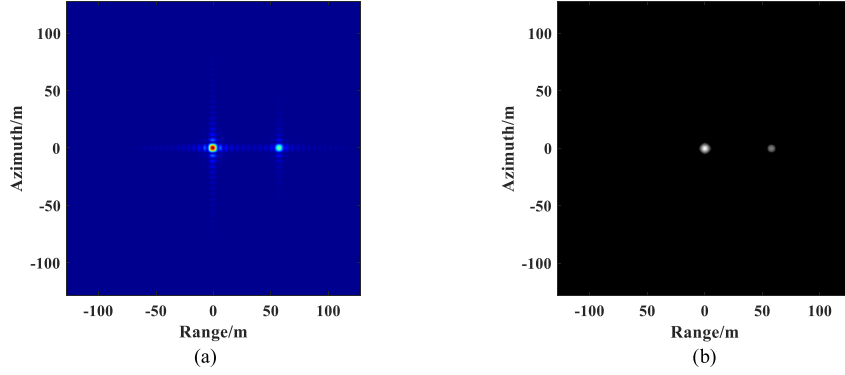


Fig. 9. Result of (a) azimuth prefocusing and (b) joint feature extraction.

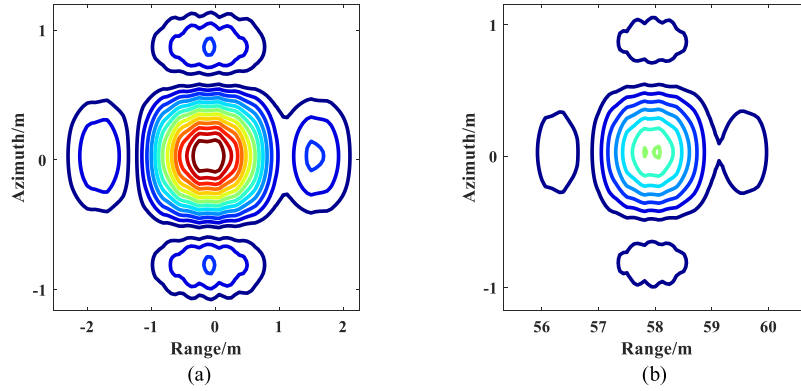


Fig. 10. 2-D IRF of scatterers of azimuth prefocusing. (a) PT1 and PT2. (b) PT3.

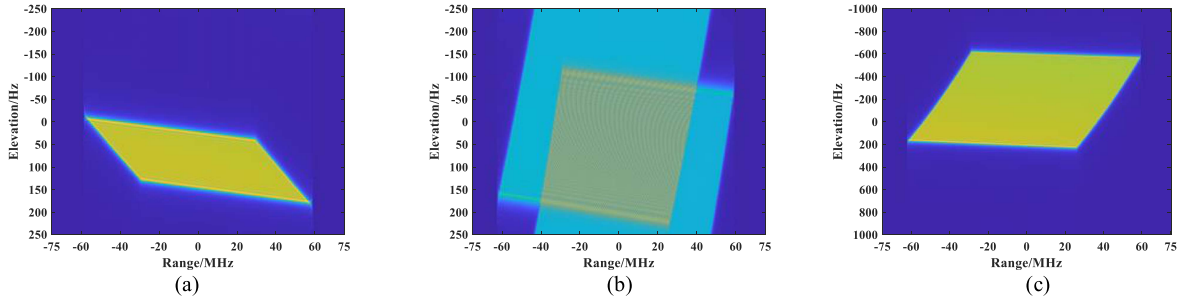


Fig. 11. Experimental results of elevation bandwidth at (a) $a = [0, 0, 0] \text{ m/s}^2$, PRF = 500 Hz, (b) $a = [2, 5, -5] \text{ m/s}^2$, PRF = 500 Hz, and (c) $a = [2, 5, -5] \text{ m/s}^2$, PRF = 2000 Hz.

every azimuth plane y_i , which are confirmed by azimuth prefocusing.

- 3) *3-D reconstruction*: Combining all focused range-elevation SAR images at certain azimuth locations, the 3-D reconstruction results of interested targets can be obtained.

V. EXPERIMENTAL RESULTS

In this section, two experiments are provided to demonstrate the effectiveness of the proposed 3-D reconstruction methods. The CLSAR system works in the spotlight mode

and the parameter settings for experiments are listed in Table II.

A. Experiment of Resolution Verification

First, in order to verify the accuracy of the resolution expression derived in (25) and the effectiveness of the proposed 3-D reconstruction approach, a simulation experiment of point targets is conducted. The simulation setting is shown in Fig. 8, in which three targets PT1, PT2, and PT3 with different elevations are located at the same azimuth cell. PT2 is set as the reference target. PT1 and PT2 have the same minimum slant range $|\mathbf{R}_{\text{ref}}|$.

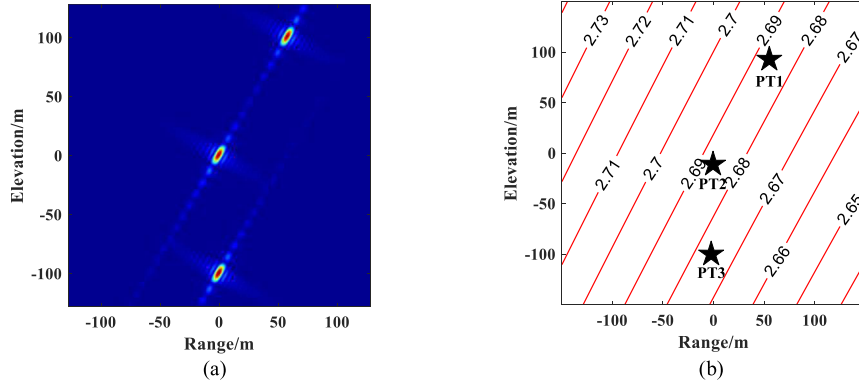


Fig. 12. Result of (a) elevation imaging and (b) theoretical calculation of elevation resolution.

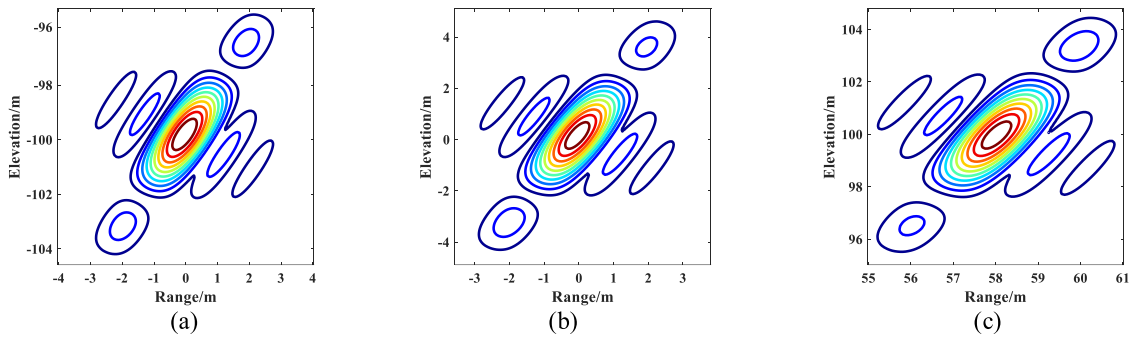


Fig. 13. 2-D IRF of scatterers of elevation focusing. (a) PT1. (b) PT2. (c) PT3.

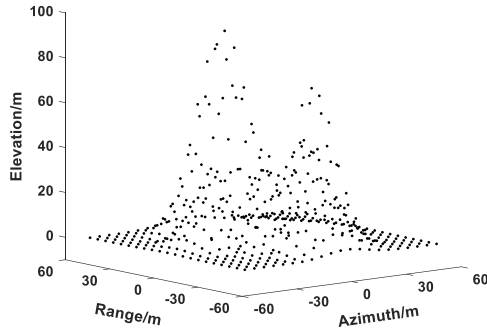


Fig. 14. Imaging scene with the same scattering intensity.

TABLE II
SIMULATION PARAMETERS

Parameter	Value
Carrier frequency	10 GHz
Pulse duration	2 μ s
Pulse bandwidth	150 MHz
Sampling frequency	200MHz
System PRF	2000Hz
Reference slant range	16km
Initial pitch angle	30°
Initial velocity vector	[0, 100, 0] m/s
Acceleration vector	[2, 5, -5] m/s ²
Time of pre-focusing sub-aperture	1 s
Time of elevation imaging sub-aperture	1 s

1) *Azimuth Prefocusing Result*: The simulation results of azimuth prefocusing and joint feature extraction are shown in Fig. 9. Note that targets with different elevations are all visually well-focused on a 2-D slant range plane [see Fig. 9(a)] and can be selected by the proposed target extraction method [see Fig. 9(b)], where PT1 and PT2 are focused at the same position and cannot be distinguished from each other since they have the same slant range history. Thus, their power is stronger than that of PT3. The results of 2-D impulse response functions (IRFs) of the targets extracted from the focused image are shown in Fig. 10 and the image quality parameters are listed in Table III. By comparing the impulse response width (IRW),

peak sidelobe ratio (PSLR), and integrated SLR (ISLR) with the ideal values, it is demonstrated that both the targets at different elevations and the reference target are well-focused. Table IV lists the 2-D coordinates (azimuth and range) of the three targets extracted from the azimuth prefocusing image and the true 2-D coordinates of these targets. Note that compared with the true coordinates, the azimuth prefocusing processing can obtain accurate azimuth coordinate information, which can be used as the assisted information in the following elevation focusing process.

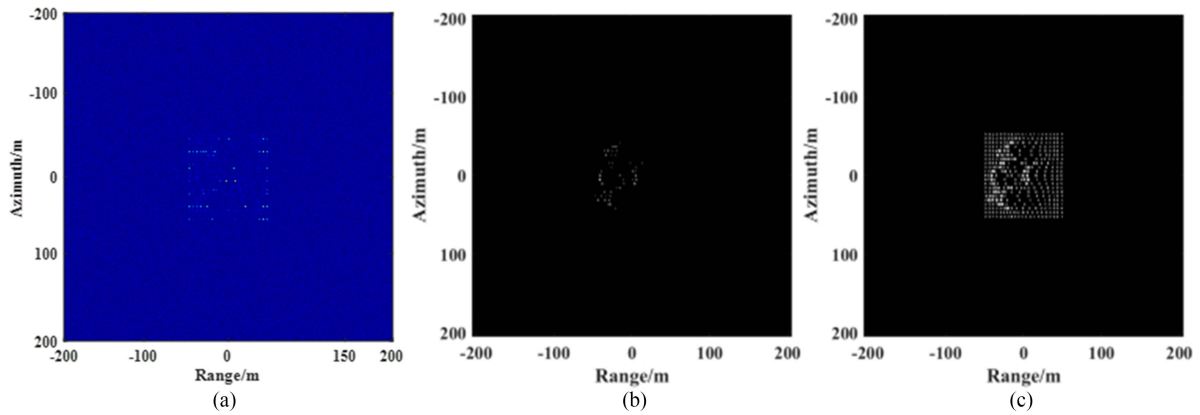


Fig. 15. Result of (a) azimuth prefocusing, (b) traditional single feature method, and (c) proposed joint feature method.

TABLE III
IMAGING QUALITY PARAMETERS OF AZIMUTH PREFOCUSING

	Range dimension			Azimuth dimension		
	IRW	PSLR	ISLR	IRW	PSLR	ISLR
Theoretical	1.10 m	-13.26 dB	-9.80 dB	0.63 m	-13.26 dB	-9.80 dB
PT1&PT2	1.12 m	-13.15 dB	-10.52 dB	0.66 m	-13.32 dB	-11.14 dB
PT3	1.12 m	-13.21 dB	-10.71 dB	0.66 m	-13.34 dB	-11.18 dB

TABLE IV
2-D COORDINATES OF AZIMUTH PREFOCUSING AND REAL SCENE

	Extracted from azimuth pre-focusing image		True coordinates of simulation	
	Azimuth	Range	Azimuth	Range
PT1	0.1 m	57.8 m	0.0 m	58.0 m
PT2	-0.05 m	-0.2 m	0.0 m	0.0 m
PT3	-0.1 m	-0.2 m	0.0 m	0.0 m

2) *Elevation Focusing Result*: After azimuth prefocusing, the azimuth planes that contain targets with different elevations can be determined. Before elevation focusing, the elevation bandwidth of the CLSAR system is simulated and illustrated in Fig. 11, where Fig. 11(a) shows the elevation bandwidth of CLSAR without 3-D acceleration, Fig. 11(b) shows the elevation bandwidth with 3-D acceleration, and Fig. 11(c) shows the elevation bandwidth after adjusting the PRF. The simulation results verify the conclusion in Section III that a small variation of acceleration can greatly affect the total elevation bandwidth. It is necessary to adjust the PRF of the system to meet the Nyquist sampling theorem in the elevation direction. According to the expressions derived in Section III, the theoretical value of fast-time resolution is determined by the bandwidth of the transmitted signal and is independent of the target's location. In contrast, the value of the elevation resolution is related to the spatial location of the target. Thus, the elevation resolution covering an area is calculated and compared with the simulation result. The elevation focusing result and the corresponding theoretical calculation result of elevation resolution are shown in Fig. 12. Note that targets located at different elevations can be well-focused due to the elevation synthetic aperture of CLSAR. Furthermore, according to Fig. 12(b), the theoretical elevation resolutions of PT1 and PT2 are both approximately

2.69 m since they have the same reference slant range. And, the theoretical elevation resolution for PT3 is approximately 2.68 m, which is slightly better than PT1 and PT2. It demonstrates that the theoretical elevation resolution changes with the target location. The 2-D IRFs of three targets PT1, PT2, and PT3 extracted from the focused elevation image are shown in Fig. 13. The image quality parameters that are extracted from the elevation focusing result are listed in Table V. Particularly, the measured values are calculated by the refined elevation profiles. Note that the elevation resolution of PT1 and PT2 is 2.70 m, and the PT3 is 2.69 m, which is close to the theoretical calculation value and confirms the theoretical analysis that the elevation resolution varies with the target's location in CLSAR. Table VI depicts the 3-D coordinates of the three targets extracted from the imaging results. Note that all targets are well-focused on the true position and the reconstruction error is negligible.

B. Experiment of Imaging Scene

Due to the lack of real data on the 3-D CLSAR system, in this experiment, the simulation results of the 3-D scene with elevation variation are examined to further evaluate the practicability of the proposed approach.

TABLE V
IMAGING QUALITY PARAMETERS OF ELEVATION IMAGING

	Range dimension			Elevation dimension		
	IRW	PSLR	ISLR	IRW	PSLR	ISLR
Theoretical	1.12 m	-13.26 dB	-9.80 dB	PT1&PT2: 2.69 m PT3: 2.68 m	-13.26 dB	-9.80 dB
PT1	1.14 m	-13.21 dB	-10.24 dB	2.70 m	-13.05 dB	-10.37 dB
PT2	1.14 m	-13.31 dB	-10.07 dB	2.70 m	-13.08 dB	-10.28 dB
PT3	1.14 m	-13.19 dB	-10.19 dB	2.69 m	-13.09 dB	-10.41 dB

TABLE VI
3-D COORDINATES OF ELEVATION FOCUSING AND REAL SCENE

	3-D coordinates extracted from elevation images			3-D coordinates of simulation point targets		
	Azimuth	Range	Elevation	Azimuth	Range	Elevation
PT1	0.1 m	58.0625 m	100.125 m	0.0 m	58.0 m	100.0 m
PT2	-0.05 m	0.0 m	0.1875 m	0.0 m	0.0 m	0.0 m
PT3	-0.1 m	0.0625 m	-99.8125 m	0.0 m	0.0 m	-100.0 m

1) *Simulation Results With the Same Scattering Intensity:* First, the imaging scene with the same scattering intensity is utilized, which is shown in Fig. 14. Note that, produced by the “peak” function of MATLAB, the imaging scene is formed by $21 \times 21 = 441$ targets. These targets are uniformly distributed in the 3-D space. The variation of the imaging scene in range, azimuth, and elevation directions are $-60-60$ m, $-60-60$ m, and $0-100$ m, respectively. After processed by the proposed approach, the results after azimuth processing are shown in Fig. 15. Among them, Fig. 15(a) represents the original azimuth pre-focusing result without feature extraction processing, Fig. 15(b) represents the result processed using the traditional extraction method based on a single feature, and Fig. 15(c) displays the result processed by the proposed joint feature extraction method. Note that although all targets have been well-focused onto the slant range imaging plane after azimuth pre-focusing, the target features are not distinct due to the presence of cluttered backgrounds, making it difficult to directly extract the azimuth information of the interested targets. After being processed by the traditional extraction method based on a single feature, only less than 100 targets with relatively strong features have been effectively extracted, causing many areas with interested targets to be mistakenly regarded as nontarget areas. However, after applying the joint feature extraction method proposed in this article, all 441 targets in the scene can be efficiently extracted, demonstrating strong robustness. Then, the elevation focusing and the 3-D reconstruction can be performed on the azimuth planes where these targets are located, and the isosurface reconstruction result is shown in Fig. 16. It is clear that the 3-D scene with elevation variation is reconstructed well.

2) *Simulation Results With Different Scattering Intensities:* Second, in order to further validate the practicality of the proposed method in real scenarios, an imaging scene with different scattering intensities is utilized, as shown in Fig. 17. This simulation experiment consists of three groups of targets with varying scattering intensities. The first group comprises nine targets uniformly distributed at 10 m intervals along the azimuth direction, centered at the point $(0, -10, 0)$. All points

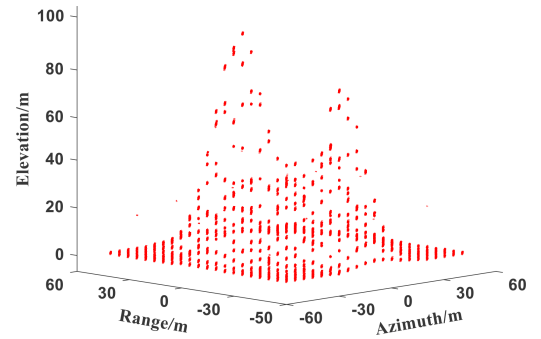


Fig. 16. Reconstructed result (the isosurface is drawn at a value of -13 dB).

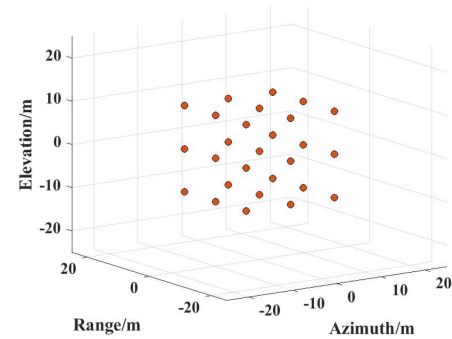


Fig. 17. Imaging scene with different scattering intensities.

in this plane have a scattering intensity of 0.5. The second group consists of nine targets with the same spacing as the first group, centered at $(0, 0, 0)$, and a scattering intensity of 1. The third group comprises nine targets with the same spacing as the previous groups, centered at $(0, 10, 0)$, and a scattering intensity of 2. The results after azimuth processing are shown in Fig. 17. Among them, Fig. 18(a) represents the result processed using the traditional extraction method based on a single feature, and Fig. 18(b) displays the result processed by the proposed joint feature extraction method. Note that, after processed by the traditional extraction method based on a single feature, only

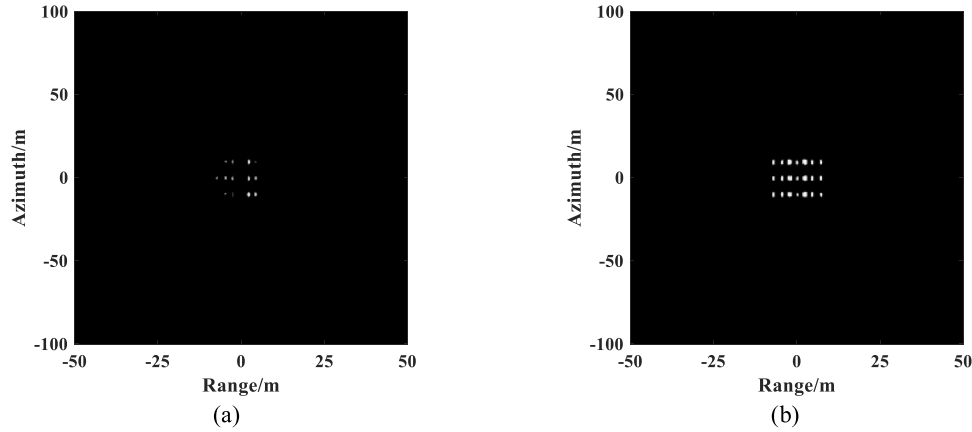


Fig. 18. Result of (a) traditional single feature method and (b) proposed joint feature method.

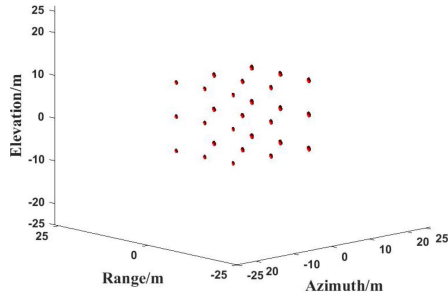


Fig. 19. Reconstructed result (the isosurface is drawn at a value of -13 dB).

half of the targets with different scattering intensities have been effectively extracted. However, after applying the joint feature extraction method proposed in this article, all 27 targets in the imaging scene can be efficiently extracted, which demonstrates that the proposed extraction method performs well even when the scattering intensity of targets in the scene varies. This further validates the robustness. After obtaining the azimuth information of targets with different scattering intensities, the elevation focusing and the 3-D reconstruction are performed, and the isosurface reconstruction result is shown in Fig. 19. It is clear that different target scattering intensities will only affect the brightness of the final reconstruction result but will not affect its 3-D reconstruction shape and accuracy.

C. Computation Burden Analyzes

The computational burden of the proposed approach is analyzed with the 3-D BP for comparison. According to the flowchart, the proposed approach mainly consists of two parts: azimuth prefocusing processing and elevation imaging processing. The azimuth prefocusing processing involves two fast-time FFT, two slow-time FFT, one Stolt interpolation, and two multiplication operations, with corresponding computational complexities of $NM \cdot \log_2 N$, $NM \cdot \log_2 M$, $2(2M_{\text{ker}} - 1)NM$, and $2NM$, respectively. N and M represent the number of sampling in the fast- and slow-time directions, and M_{ker} is the length of the interpolation function. The elevation imaging processing uses the 2-D BPA, with a computational complexity

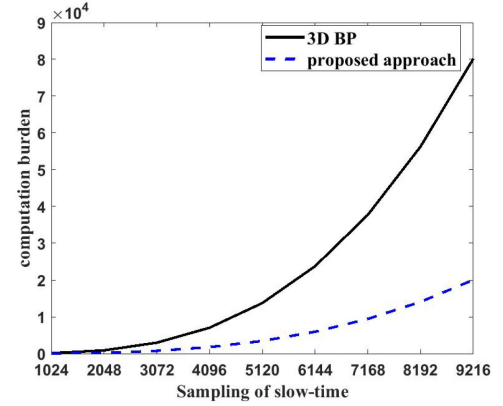


Fig. 20. Computation burdens of the proposed approach and 3-D BP.

TABLE VII
COMPUTATIONAL TIME COMPARISON

	Proposed approach	Traditional 3-D BP
Computational time	266.87 s	32836.36 s

of δNM^2 , where δ represents the azimuth sparse factor of the interested targets in the scene. Therefore, the computational burden of the proposed method can be derived as

$$O_{\text{pro}} = NM \cdot \log_2 NM + NM + 2(2M_{\text{ker}} - 1)NM + \delta NM^2. \quad (36)$$

The computational burdens of the proposed method and 3-D BP algorithm ($O_{3D} = NM^3$) under different slow-time sampling numbers are shown in Fig. 20, where fast-time sampling number $N = 2048$ and azimuth sparse factor $\delta = 0.4$. Note that due to eliminating a large number of nontarget regions through azimuth prefocusing, the computational burden of the proposed approach is far less than that of the 3-D BP algorithm. Moreover, the computational time of the proposed approach and the traditional 3-D BP is compared in Table VII, which is performed on a computer equipped with an Intel(R) Core(TM) i7-1165G7

processor, 16 GB of memory, and MATLAB 2022(a). Due to the excessively high computational complexity of the 3-D BP algorithm, we only conducted one set of experiments. Note that the computational time of the proposed method is much shorter than that of the traditional 3-D BP algorithm, which effectively enhances the practical value of the 3-D CLSAR system.

VI. CONCLUSION

As an application in remote sensing, SAR shows an advantage in target reconstruction because of its high resolution. However, the traditional single-channel straight path SAR system cannot obtain true 3-D coordinates of the targets due to cylindrical symmetry. To solve this problem, in this article, a novel 3-D reconstruction approach for a single-channel CLSAR system has been proposed. First, the 3-D model of the CLSAR system has been presented with the vector notation, with which the highly accurate expression of range history is listed. On this basis, the parameters of CLSAR include: 1) total bandwidth, i.e., azimuth bandwidth and elevation bandwidth; and 2) resolutions, i.e., spatial resolution and vertical plane resolution have been analyzed. Second, the approach of the 3-D reconstruction based on the azimuth prefocusing is presented. Our key is that the horizontal subaperture data utilized for azimuth prefocusing are separated out from the curved full-aperture to confirm assisted azimuth coordinates of interested targets in the observing scene. With the use of this assisted information, the elevation image of the scene can be constructed by employing the elevation synthetic aperture of CLSAR, and the accurate 3-D coordinates of targets can be extracted. Our theoretical analysis is corroborated and the applicability is evaluated via numerical experiments.

REFERENCES

- [1] D. A. Ausherman, A. Kozma, J. L. Walker, H. M. Jones, and E. C. Poggio, "Developments in radar imaging," *IEEE Trans. Aerosp. Electron. Syst.*, vol. AES-20, no. 4, pp. 363–400, Jul. 1984.
- [2] W. G. Carrara, R. S. Goodman, and R. M. Majewski, *Spotlight Synthetic Aperture Radar: Signal Processing Algorithms*. Norwood, MA, USA: Artech House, 1995.
- [3] J. C. Curlander and R. N. McDonough, *Synthetic Aperture Radar: Systems and Signal Processing*. Hoboken, NJ, USA: Wiley, 1991.
- [4] I. G. Cumming and F. H. Wong, *Digital Processing of Synthetic Aperture Radar Data: Algorithms and Implementation*. Boston, MA, USA: Artech House, 2005.
- [5] K. S. Chen, *Principles of Synthetic Aperture Radar Imaging: A System Simulation Approach*. Boca Raton, FL, USA: CRC, 2016.
- [6] Y. Liu et al., "Echo model analyses and imaging algorithm for high-resolution SAR on high-speed platform," *IEEE Trans. Geosci. Remote Sens.*, vol. 50, no. 3, pp. 933–950, Mar. 2012.
- [7] O. Frey, C. Magnard, M. Rüegg, and E. Meier, "Focusing of airborne synthetic aperture radar data from highly nonlinear flight tracks," *IEEE Trans. Geosci. Remote Sens.*, vol. 47, no. 6, pp. 1844–1858, Jun. 2009.
- [8] W. L. Ran, Z. Liu, T. Zhang, and T. Li, "Autofocus for correcting three-dimensional trajectory deviations in synthetic aperture radar," in *Proc. IEEE CIE Int. Conf. Radar*, 2016, pp. 1–4.
- [9] M. L. Bryant, L. L. Gostin, and M. Soumekh, "3-D E-CSAR imaging of a T-72 tank and synthesis of its SAR reconstructions," *IEEE Trans. Aerosp. Electron. Syst.*, vol. 39, no. 1, pp. 211–227, Jan. 2003.
- [10] G. Xu, B. Zhang, H. Yu, J. Chen, M. Xing, and W. Hong, "Sparse synthetic aperture radar imaging from compressed sensing and machine learning: Theories, applications and trends," *IEEE Geosci. Remote Sens. Mag.*, vol. 10, no. 4, pp. 32–69, Dec. 2022.
- [11] R. Bamler and P. Hartl, "Synthetic aperture radar interferometry—Topical review," *Inverse Probl.*, vol. 14, no. 4, pp. R1–R54, 1998.
- [12] A. Ferretti, C. Prati, and F. Rocca, "Permanent targets in SAR interferometry," *IEEE Trans. Geosci. Remote Sens.*, vol. 39, no. 1, pp. 8–20, Jan. 2001.
- [13] P. A. Rosen et al., "Synthetic aperture radar interferometry," *Proc. IEEE*, vol. 88, no. 3, pp. 333–382, Mar. 2000.
- [14] S. Gernhardt, N. Adam, M. Eineder, and R. Bamler, "Potential of very high-resolution SAR for persistent target interferometry in urban areas," *Ann. GIS*, vol. 16, no. 2, pp. 103–111, Jun. 2010.
- [15] A. Reigber and A. Moreira, "First demonstration of airborne SAR tomography using multibaseline L-band data," *IEEE Trans. Geosci. Remote Sens.*, vol. 38, no. 5, pp. 2142–2152, Sep. 2000.
- [16] G. Ferraiuolo, F. Meglio, V. Pascasio, and G. Schirinzi, "DEM reconstruction accuracy in multi-channel SAR interferometry," *IEEE Trans. Geosci. Remote Sens.*, vol. 47, no. 1, pp. 191–201, Jan. 2009.
- [17] X. Zhu and R. Bamler, "Very high resolution spaceborne SAR tomography in urban environment," *IEEE Trans. Geosci. Remote Sens.*, vol. 48, no. 12, pp. 4296–4308, Dec. 2010.
- [18] A. Budillon, A. Evangelista, and G. Schirinzi, "Three-dimensional SAR focusing from multipass signals using compressive sampling," *IEEE Trans. Geosci. Remote Sens.*, vol. 49, no. 1, pp. 488–499, Jan. 2011.
- [19] B. Zhang, G. Xu, R. Zhou, H. Zhang, and W. Hong, "Multi-channel back-projection algorithm for mmWave Automotive MIMO SAR imaging with doppler-division multiplexing," *IEEE J. Sel. Topics Signal Process.*, vol. 17, no. 2, pp. 445–457, Mar. 2023.
- [20] G. Fornaro, F. Lombardini, and F. Serafino, "Three-dimensional multipass SAR focusing: Experiments with long-term spaceborne data," *IEEE Trans. Geosci. Remote Sens.*, vol. 43, no. 4, pp. 702–714, Apr. 2005.
- [21] M. Ponce, P. Prats-Iraola, R. Scheiber, A. Reigber, and A. Moreira, "First airborne demonstration of holographic SAR tomography with fully polarimetric multicircular acquisitions at L-band," *IEEE Trans. Geosci. Remote Sens.*, vol. 54, no. 10, pp. 6170–6196, Oct. 2016.
- [22] J. Fortuny-Guasch and J. M. Lopez-Sanchez, "Extension of the 3-D range migration algorithm to cylindrical and spherical scanning geometries," *IEEE Trans. Antennas Propag.*, vol. 49, no. 10, pp. 1434–1444, Oct. 2001.
- [23] Z. Su, Y. Peng, and X. Wang, "Fast non-iterative imaging algorithm for CLSAR," in *Proc. IEEE Int. Radar Conf.*, 2005, pp. 778–782.
- [24] Z. Su, Y. Peng, and X. Wang, "Non-iterative imaging algorithm for CLSAR," in *IEEE Int. Conf. Acoust., Speech, Signal Process.*, 2005, vol. 2, pp. 577–580.
- [25] R. Xiaozhen and Y. Ruliang, "A method for CLSAR 3-D imaging based on backprojection and beamforming," in *Proc. 2nd Asian-Pacific Conf. Synthetic Aperture Radar*, 2009, pp. 1022–1025.
- [26] K. Knaell, "Three-dimensional SAR from curvilinear apertures," in *Proc. IEEE Nat. Radar Conf.*, 1996, pp. 220–225.
- [27] K. Knaell, "Advances in three-dimensional SAR from curvilinear apertures," in *Proc. SPIE, Radar Process., Technol., Appl. II*, 1997, pp. 178–184.
- [28] J. Li, Z. Bi, Z.-S. Liu, and K. Kriaell, "Use of curvilinear SAR for three-dimensional target feature extraction," *IEE Proc., Radar, Sonar Navig.*, vol. 144, no. 5, pp. 275–283, Oct. 1997.
- [29] J. Fortuny-Guasch and J. M. Lopez-Sanchez, "Extension of the 3-D range migration algorithm to cylindrical and spherical scanning geometries," *IEEE Trans. Antennas Propag.*, vol. 49, no. 10, pp. 1434–1444, Oct. 2001.
- [30] Z. Su, R. Wu, J. Liu, and J. Liu, "A robust autofocus algorithm for the 3-D target feature extraction in curvilinear SAR," in *Proc. CIE Int. Conf. Radar Process.*, 2001, pp. 644–648.
- [31] K. Goel and N. Adam, "Three-dimensional positioning of point targets based on radargrammetry," *IEEE Trans. Geosci. Remote Sens.*, vol. 50, no. 6, pp. 2355–2363, Jun. 2012.
- [32] P. Capaldo, M. Crespi, F. Fratarcangeli, A. Nascetti, and F. Pieralice, "High-resolution SAR radargrammetry: A first application with COSMO-SkyMed spotLight imagery," *IEEE Geosci. Remote Sens. Lett.*, vol. 8, no. 6, pp. 1100–1104, Nov. 2011.
- [33] H. Raggam, K. Gutjahr, R. Perko, and M. Schardt, "Assessment of the stereo-radargrammetric mapping potential of TerraSAR-X multi-beam spotlight data," *IEEE Trans. Geosci. Remote Sens.*, vol. 48, no. 2, pp. 971–977, Feb. 2010.
- [34] S. Tang, L. Zhang, P. Guo, G. Liu, and G. Sun, "Acceleration model analyses and imaging algorithm for highly squinted airborne spotlight-mode SAR with maneuvers," *IEEE J. Sel. Topics Appl. Earth Observ. Remote Sens.*, vol. 8, no. 3, pp. 1120–1131, Mar. 2015.
- [35] P. Guo, L. Zhang, and S. Tang, "Resolution calculation and analysis in high-resolution spaceborne SAR," *Electron. Lett.*, vol. 51, no. 15, pp. 1199–1201, Jul. 2015.

- [36] J. Chen, M. Xing, X.-G. Xia, J. Zhang, B. Liang, and D.-G. Yang, "SVD-based ambiguity function analysis for nonlinear trajectory SAR," *IEEE Trans. Geosci. Remote Sens.*, vol. 59, no. 4, pp. 3072–3087, Apr. 2021.
- [37] J. Chen, G.-C. Sun, Y. Wang, L. Guo, M. Xing, and Y. Gao, "An analytical resolution evaluation approach for bistatic GEOSAR based on local feature of ambiguity function," *IEEE Trans. Geosci. Remote Sens.*, vol. 56, no. 4, pp. 2159–2169, Apr. 2018.
- [38] M. Soumekh, *Synthetic Aperture Radar Signal Processing: With MATLAB Algorithms*. New York: Wiley, 1999.
- [39] S. Tang, P. Guo, L. Zhang, and H. C. So, "Focusing hypersonic vehicle-borne SAR data using radius/angle algorithm," *IEEE Trans. Geosci. Remote Sens.*, vol. 58, no. 1, pp. 281–293, Jan. 2020.
- [40] F. He, Y. Yang, Z. Dong, and D. Liang, "Progress and prospects of curvilinear SAR 3-D imaging," *J. Radars*, vol. 4, no. 2, pp. 130–135, 2015.
- [41] S. Tang, C. Lin, Y. Zhou, H. C. So, L. Zhang, and Z. Liu, "Processing of long integration time spaceborne SAR data with curved orbit," *IEEE Trans. Geosci. Remote Sens.*, vol. 56, no. 2, pp. 888–904, Feb. 2018.



Chenghao Jiang was born in Xi'an, Shaanxi Province, China. He received the B.S. degree in information engineering from Xi'an Jiaotong University, Xi'an, China, in 2016, and the Ph.D. degree in electrical engineering from Xidian University, Xi'an, in 2023.

His research interests include radar signal processing and 3-D SAR imaging.



Shiyang Tang (Member, IEEE) was born in Jiangsu Province, China. He received the B.S. and Ph.D. degrees in electrical engineering from Xidian University, Xi'an, China, in 2011 and 2016, respectively.

He is a Full Professor with the National Key Laboratory of Radar Signal Processing, Xidian University. His research interests include imaging of SAR with curved paths and high-speed moving target detection and imaging.



Qi Dong was born in Chifeng, China. She received the Ph.D. degree in electronic engineering from Xidian University, Xi'an, China, in 2018.

She is currently an Electrical Engineer with the Beijing Control and Electronic Technology Research Institute. Her research interests include synthetic aperture radar imaging, SAR system radar forward-looking imaging, and SAR-GMTI.



Yinan Li (Member, IEEE) was born in Xi'an, Shaanxi, China. He received the Ph.D. degree in electrical engineering from Xidian University, Xi'an, China, in 2023.

He is currently a Professor with the China Academy of Space Technology, Xi'an. His research interests include the system design and calibration. He has participated in the development of the microwave radiometers for the FY-3 satellite and HY-2 satellite successively. He is also the Chief Designer, developing the synthetic aperture radiometer for the

ocean salinity satellite of China.



Juan Zhang received the Ph.D. degree in electrical engineering from Xidian University, Xi'an, China, in 2010.

In 2014, she was a Visiting Scholar at Nanyang Technological University (NTU), Singapore. She is currently a Professor with the National Key Laboratory of Radar Signal Processing, Xidian University. Her research interests include adaptive signal processing, radar electronic counter measure, and radar system designation and simulation.



Guoliang Sun was born in Jiangsu, China. He received the B.S. degree in electrical engineering from the Nanjing University of Science and Technology (NJUST), Nanjing, China, in 2005, and the Advanced Master's degree in electrical engineering from the Institut Supérieur de l'Aéronautique et de l'Espace (ISAE), Toulouse, France, in 2012.

He is currently a Professor of Senior Engineer with Letri, Avic. His research interests include radar system, SAR signal processing, etc.



Linrang Zhang was born in Shaanxi Province, China, in 1966. He received the M.S. and Ph.D. degrees in electrical engineering from Xidian University, Xi'an, China, in 1991 and 1999, respectively.

He is a Full Professor with the National Key Laboratory of Radar Signal Processing, Xidian University. He has authored or coauthored three books and more than 100 papers. His research interests include radar system analysis and simulation, radar signal processing, and jamming suppression.